In vitro interaction assay

Interaction between Smac and XIAP-BIR3 was examined by GST-mediated pull-down assays. Approximately 0.4 mg of a wild-type or mutant BIR3 fragment was bound to 200 μl of glutathione resin as a GST-fusion protein and incubated with 0.5 mg of wild-type or mutant Smac at room temperature. After extensive washing with an assay buffer containing 25 mM Tris, pH 8.0, 150 mM NaCl, and 2 mM dithiothreitol (DTT), the complex was eluted with 5 mM reduced glutathione and visualized by SDS-polyacrylamide gel electrophoresis (SDS-PAGE) with Coomassie staining.

Crystallization and data collection

Crystals were grown by the hanging-drop vapour-diffusion method by mixing the Smac/XIAP-BIR3 complex (15 mg ml^{-1}) with an equal volume of reservoir solution. At 4 °C, the reservoir contained 100 mM MES buffer, pH 6.5, 12% isopropanol (v/v), 200 mM sodium citrate, and 10 mM DTT. At 23 °C, the reservoir contained 100 mM citrate buffer, pH 5.5, 5% PEG 4000 and 10% isopropanol. Crystals appeared after 1–4 days and reached a maximum size over a period of 1–3 weeks. Both crystals are in the triclinic space group P1 and contain two complexes in each unit cell. However, the unit cell dimensions are significantly different. Crystals grown at 4 °C have a = 47.0 Å, b = 54.6 Å, c = 74.2 Å, α = 93.0°, β = 101.1°, and γ = 94.9°; crystals grown at 23 °C have a = 48.1 Å, b = 52.9 Å, c = 67.1 Å, α = 100.0°, β = 104.1°, and γ = 94.0.° Diffraction data were primarily collected using an R-AXIS-IV imaging plate detector mounted on a Rigaku 200HB generator. Derivatives were obtained by soaking crystals in reservoir buffer containing 20% glycerol (v/v) and heavy atoms. The concentration and soaking time for mercury thimerosal were 1 mM and 20 hours, respectively. To collect data at −170 °C, crystals were equilibrated in a cryoprotectant buffer containing reservoir buffer plus 20% glycerol (v/v) and were flash frozen in a cold nitrogen stream. The high-resolution native data were collected at the NSLS beamline X4A.

Structure determination

We focused on the crystals grown at 4 °C first, because of the availability of a high-quality selenomethionine derivative. The first six selenium positions were determined using SOLVE[21] and further refined using MLPHARE[22]. The positions of the other four selenium atoms and mercury thimerosal were identified using difference Fourier methods. Initial MIR phases calculated with the program MLPHARE[22] had a mean figure of merit of 0.404 to 3.0 Å resolution, and were improved with solvent flattening and histogram matching using the program DM[22]. The electron density for the Smac N-terminal four residues was very clear in the experimental map. A model was built into MIR electron density with the program O[23] and refined at 2.6 Å resolution by simulated annealing using the program XPLOR[24]. Non-crystallography symmetry (NCS) constraints were applied to all refinement cycles except the last one. The two refined complexes (R factor 24% and free R 28.5%) are nearly identical to one another, and contain Smac residues 1–6 and 13–157, XIAP residues 251–343, and 58 ordered water molecules. Residues 7–12 and 158–162 in Smac and the terminal residues in XIAP (238–250 and 344–358) have no electron density in the maps, and we presume that these regions are disordered in the crystals. After completion of the refinement for the crystals grown at 4 °C, the atomic coordinates of BIR3 and Smac were used individually to obtain molecular replacement solutions for the crystals grown at 23 °C, using AMoRe[25]. The solutions were combined in O[23]. Rigid body refinement by XPLOR[24] confirmed the correctness of the solutions. This model was further refined at 2.0 Å resolution by simulated annealing using the program XPLOR[24], followed by model building in O[23]. NCS was helpful for the initial cycles of refinement. The final refined model, with an R factor of 22.7% and free R of 26.8%, contains two complexes. One complex contains Smac 1–157 and XIAP 256–357, and the other complex contains Smac 1–157 and XIAP 256–343. Except for the C-terminal 14 residues of XIAP in the first complex, which is disordered in the second one, the structures of these two complexes are identical to one another.

Received 18 September; accepted 9 November 2000.

1. Steller, H. Mechanisms and genes of cellular suicide. *Science* **267,** 1445–1449 (1995).
2. Jacobson, M. D., Weil, M. & Raff, M. C. Programmed cell death in animal development. *Cell* **88,** 347–354 (1997).
3. Hengartner, M. O. Programmed cell death in invertebrates. *Curr. Opin. Genet. Dev.* **6,** 34–38 (1996).
4. Horvitz, H. R. Genetic control of programmed cell death in the nematode *Caenorhabditis elegans*. *Cancer Res.* **59,** 1701–1706 (1999).
5. Deveraux, Q. L. & Reed, J. C. IAP family proteins—suppressors of apoptosis. *Genes Dev.* **13,** 239–252 (1999).
6. Miller, L. K. An exegesis of IAPs: salvation and surprises from BIR motifs. *Trends Cell Biol.* **9,** 323–328 (1999).
7. Du, C., Fang, M., Li, Y. & Wang, X. Smac, a mitochondrial protein that promotes cytochrome c-dependent caspase activation during apoptosis. *Cell* **102,** 33–42 (2000).
8. Verhagen, A. M. *et al.* Identification of DIABLO, a mammalian protein that promotes apoptosis by binding to and antagonizing IAP proteins. *Cell* **102,** 43–53 (2000).
9. Chai, J. *et al.* Structural and biochemical basis of apoptotic activation by Smac/DIABLO. *Nature* **406,** 855–862 (2000).
10. Deveraux, Q. L. *et al.* Cleavage of human inhibitor of apoptosis protein XIAP results in fragments with distinct specificities for caspases. *EMBO J.* **18,** 5242–5251 (1999).
11. Takahashi, R. *et al.* A single BIR domain of XIAP sufficient for inhibiting caspases. *J. Biol. Chem.* **273,** 7787–7790 (1998).
12. Sun, C. *et al.* NMR structure and mutagenesis of the inhibitor-of-apoptosis protein XIAP. *Nature* **401,** 818–822 (1999).
13. Sun, C. *et al.* NMR structure and mutagenesis of the third BIR domain of the inhibitor of apoptosis protein XIAP. *J. Biol. Chem* **275,** 33777–33781 (2000).
14. Shi, Y. Survivin structure: crystal unclear. *Nature Struct. Biol.* **7,** 620–623 (2000).
15. Verdecia, M. A. *et al.* Structure of the human anti-apoptotic protein survivin reveals a dimeric arrangement. *Nature Struct. Biol.* **7,** 602–608 (2000).
16. Chantalat, L. *et al.* Crystal structure of human survivin reveals a bow-tie-shaped dimer with two unusual alpha helical extensions. *Mol. Cell* **6,** 183–189 (2000).
17. Wang, S., Hawkins, C., Yoo, S., Muller, H.-A. & Hay, B. The *Drosophila* caspase inhibitor DIAP1 is essential for cell survival and is negatively regulated by HID. *Cell* **98,** 453–463 (1999).
18. Goyal, L., McCall, K., Agapite, J., Hartwieg, E. & Steller, H. Induction of apoptosis by *Drosophila* reaper, hid and grim through inhibition of IAP function. *EMBO J.* **19,** 589–597 (2000).
19. Hirel, P.-H., Schmitter, J.-M., Dessen, P., Fayat, G. & Blanquet, S. Extent of N-terminal methionine excision from *Escherichia coli* proteins is governed by the side-chain length of the penultimate amino acid. *Proc. Natl Acad. Sci. USA* **86,** 8247–8251 (1989).
20. Lisi, S., Mazzon, I. & White, K. Diverse domains of THREAD/DIAP1 are required to inhibit apoptosis induced by REAPER and HID in *Drosophila*. *Genetics* **154,** 669–678 (2000).
21. Terwilliger, T. C. & Berendzen, J. Correlated phasing of multiple isomorphous replacement data. *Acta Crystallogr. D* **52,** 749–757 (1996).
22. Collaborative Computational Project. The CCP4 suite: programs for protein crystallography. *Acta Crystallogr. D.* **50,** 760–763 (1994).
23. Jones, T. A., Zou, J.-Y., Cowan, S. W. & Kjeldgaard, M. Improved methods for building protein models in electron density maps and the location of errors in these models. *Acta Crystallogr. A* **47,** 110–119 (1991).
24. Brunger, A. T. *X-PLOR, a System for Crystallography and NMR* (Yale Univ. Press, New Haven, Connecticut, 1991).
25. Navaza, J. AMoRe: an automated package for molecular replacement. *Acta Crystallogr. A* **50,** 157–163 (1994).
26. Klaulis, P. J. Molscript: a program to produce both detailed and schematic plots of protein structures. *J. Appl. Crystallogr.* **24,** 946–950 (1991).
27. Nicholls, A., Sharp, K. A. & Honig, B. Protein folding and association: insights from the interfacial and thermodynamic properties of hydrocarbons. *Proteins: Struct. Funct. Genet.* **11,** 281–296 (1991).

Supplementary information is available on *Nature*'s World-Wide Web site (http://www.nature.com) or as paper copy from the London editorial office of *Nature*.

Acknowledgements

We thank C. Ogata for help at the NSLS-X4A beamline; F. Hughson for critically reading the manuscript; S. Kyin for peptide sequencing, DNA synthesis and mass spectroscopy; and N. Hunt for secretarial assistance. This research is supported by start-up funds from Princeton University (Y.S.) and the Howard Hughes Medical Institute (X.W.). Y.S. is a Searle Scholar and a Rita Allen Scholar.

Correspondence and requests for materials should be addressed to Y.S. (e-mail: yshi@molbio.princeton.edu). Atomic coordinates for the Smac/BIR3 complex have been deposited at the Protein Data Bank with accession number 1G73.

correction

Digital selection and analogue amplification coexist in a cortex-inspired silicon circuit

Richard H. R. Hahnloser, Rahul Sarpeshkar, Misha A. Mahowald, Rodney J. Douglas & H. Sebastian Seung

Nature **405,** 947–951 (2000).

There were two errors in the reference list of this paper. Reference 22 should have been:

Sharpeshkar, R. Analog versus digital: extrapolating from electronics to neurobiology. *Neural Comput.* **10,** 1601–1638 (1998).

Also, the following reference was omitted but should have been cited along with refs 5–9 at the top of page 948.

Douglas R. J., Koch, C., Mahowald, M. A., Martin, K. A. C. & Suarez, H. Recurrent excitation in neocortical circuits. *Science* **269,** 981–985 (1995). □

16. Tunnicliffe, V., McArthur, A. G. & McHugh, D. A biogeographical perspective of the deep-sea hydrothermal vent fauna. *Adv. Mar. Biol.* **34,** 353–442 (1998).
17. Sibuet, M. & Olu, K. Biogeography, biodiversity and fluid dependence of deep-sea cold-seep communities at active and passive margins. *Deep-Sea Res. II* **45,** 517–567 (1998).
18. Heezen, B. C. & Tharp, M. *World Ocean Floor* (Map). United States Navy, Office of Naval Research (Washington, D.C., 1977).
19. Bouchet, P. & Metivier, B. Living Pleurotomariidae (Mollusca: Gastropoda) from the South Pacific. *New Zealand J. Zoo.*, **9,** 309–318 (1982).
20. Ameziane-Cominardi, N., Bourseau, J. P. & Roux, M. Les crinoides pedoncules de Nouvelle-Caledonie (S.W. Pacifique) : une faune ancestrale issue de la Mesogee mesozoique. *C.R. Acad. Sc. Paris*, **304,** 15–18 (1987).
21. Laurin, B. Decouverte d'un squelette de soutien du lophophore de type "crura" chez un brachiopode inarticule : description de Neoancistrocrania norfolki gen. sp. nov. (Cranidae). *C.R. Acad. Sci. Paris*, **314,** 343–350 (1992).
22. Richer de Forges, B. La Diversite du Benthos Marin de Nouvelle-Caledonie: de l'Espece a la Notion de Patrimonine. PhD Thesis, Museum National d'Histoire Naturelle, Paris (1998).
23. Vacelet, J. *et al.* A colonial sphinctozoan sponge related to Triassic reef builders surviving in deep water off New Caledonia. *C.R. Acad. Sci.* **314,** 379–385 (1992).
24. Grigg, R. W. Resource management of precious corals: a review and application to shallow water reef-building corals. *Marine Ecol.* **5,** 57–74 (1984).
25. Pielou, E. C. in *Population and Community Ecology* 311–312 (Gordon and Breach Science, New York, 1974).
26. Richer de Forges, B. in *Resultats des Campagnes MUSORSTOM.* Volume 10 (ed. Crosnier, A.) *Mem. Mus. Natl Hist. Nat.* **156,** 475–491 (1993).
27. Koslow, J. A. Community structure in North Atlantic deep-sea fishes. *Prog. Oceanogr.* **31,** 321–338 (1993).

Acknowledgements

Results from the northern Tasman Sea were obtained as part of the MUSORSTOM program, a collaboration between ORSTOM and the Natural History Museum in Paris, and involved some 181 researchers from 92 Institutions and 24 nations. Work around Tasmania was supported by CSIRO and grants from Environment Australia and the Fisheries Research Development Corporation and involved 25 researchers. Their contributions are gratefully acknowledged; in particular, we thank R. Grandperrin, A. Crosnier, P. Bouchet, K. Gowlett-Holmes, M. Lewis, S. Cummings, J.S. Philippe and the crews of the RV *Alis* and *Southern Surveyor.* J.A.K. received support from a National Research Council Senior Research Fellowship.

Correspondence and requests for materials should be addressed to J.A.K. (e-mail: tony.koslow@marine.csiro.au).

Digital selection and analogue amplification coexist in a cortex-inspired silicon circuit

Richard H. R. Hahnloser*‡, Rahul Sarpeshkar†§, Misha A. Mahowald*, Rodney J. Douglas* & H. Sebastian Seung†‡

** Institute of Neuroinformatics ETHZ/UNIZ, Winterthurerstrasse 190, 8057 Zürich, Switzerland*
† Bell Laboratories, Murray Hill, New Jersey 07974, USA
‡ Department of Brain and Cognitive Sciences and § Department of Electrical Engineering and Computer Science, MIT, Cambridge, Massachusetts 02139, USA

Digital circuits such as the flip-flop use feedback to achieve multistability and nonlinearity to restore signals to logical levels, for example 0 and 1. Analogue feedback circuits are generally designed to operate linearly, so that signals are over a range, and the response is unique. By contrast, the response of cortical circuits to sensory stimulation can be both multistable and graded[1–4]. We propose that the neocortex combines digital selection of an active set of neurons with analogue response by dynamically varying the positive feedback inherent in its recurrent connections. Strong positive feedback causes differential instabilities that drive the selection of a set of active neurons under the constraints embedded in the synaptic weights. Once selected, the active neurons generate weaker, stable feedback that provides analogue amplification of the input. Here we present our model of cortical processing as an electronic circuit that emulates this hybrid operation, and so is able to perform computations that are similar to stimulus selection, gain modulation and spatio-temporal pattern generation in the neocortex.

The multistability of digital circuits and the linear amplification achieved in analogue circuits are generally seen as incompatible functions and are separated into two classes of electronic technology. However, the neuronal circuits of the neocortex do not respect this distinction. There, multistability coexists with analogue response. For example, when a visual stimulus is attended at the expense of other visual stimuli—the subject is concentrating on one object in a field of vision—then many cortical neurons tend to respond in a graded way to the sensory attributes of the attended stimulus, as if it were presented alone[2].

We have designed a simple electronic circuit that emulates this hybrid behaviour. The circuit comprises a ring of 16 excitatory neurons, each of which makes synaptic connections of variable strength onto itself and onto its nearest and next nearest neighbours. These localized excitatory interactions reflect the preference for local connections observed in neocortex. At the centre of the ring is a single inhibitory neuron that receives synaptic input from all the

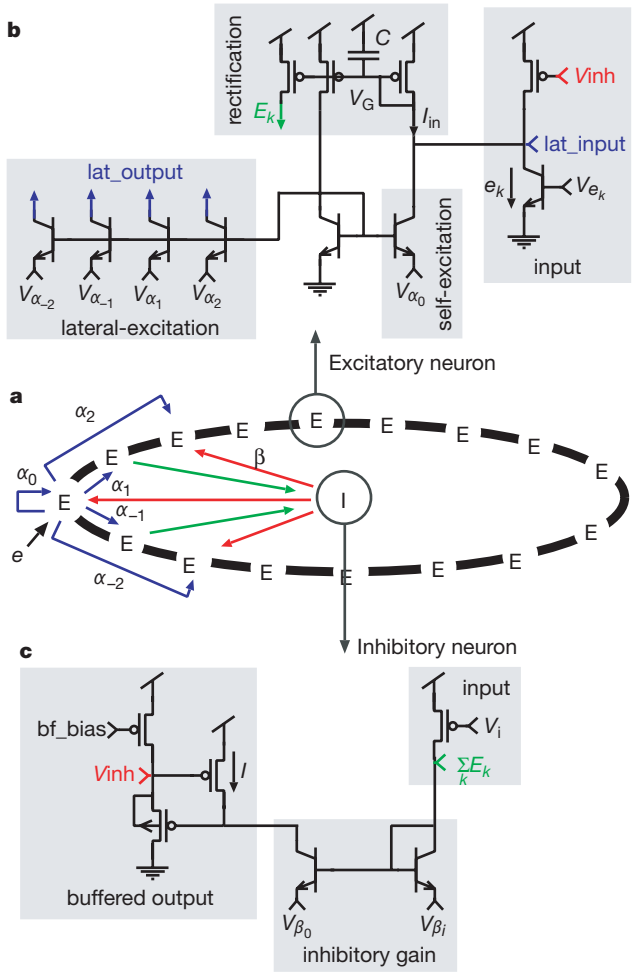

Figure 1 Silicon implementation of a recurrent network with a ring architecture. The synaptic connections are consistently coloured in the **a**–**c**. **a**, Each excitatory neuron E makes connections (blue) with itself and four neighbours on the ring, of strength α_i. The inhibitory neuron I makes global recurrent connections on the ring of strength β. Green, presynaptic connections; red, postsynaptic connections. **b**, The core of the excitatory neuron is the current mirror labelled rectification which contains a large capacitance. **c**, The core of the inhibitory neuron is the bipolar current mirror that sets the gain of inhibition (see Methods).

excitatory neurons, and returns inhibition to them. This simple architecture and similar variants have been used previously to model response properties of neurons in cortex[5–9] and other[10–12] brain areas.

The output of each excitatory neuron is an electrical current that is positive if the neuron is active, and zero if it is inactive. Negative values are not possible, because the artificial neurons are based on current mirrors, which have a rectification nonlinearity (Fig. 1b, rectification).

Each excitatory neuron can be stimulated independently by an electrical current. The response of the population to stimulation of a single neuron is shown in Fig. 2a (red line). The response profile is centred on the stimulus and extends over a large fraction of the ring. In this way, the output currents of the circuit form a distributed representation of stimulus location. In many brain areas[8], such distributed representations have been observed and been referred to as population codes[13,14]. In our circuit, the population code arises by recurrent excitation, which causes spreading of activity in both directions, until it is cut off by recurrent inhibition. Beyond this cut-off, the excitation is not strong enough to overcome the threshold for activation set by inhibition.

To generate Fig. 2a, the stimulus was fixed, and the responses of all the neurons were measured. A similar graph is obtained if the response of a particular neuron is plotted as a function of the location of the stimulus, which is the traditional procedure used by electrophysiologists to map a receptive field or the tuning curve of a cell. Neurons can maintain their tuning to a sensory variable, such as stimulus orientation or retinal location, but respond with an amplitude that is modulated by another variable, such as eye position or attention. Our circuit exhibits this remarkable phenomenon, called gain modulation, when a uniform background excitation is applied in addition to the fixed localized stimulus.

When we changed the amplitude of the background, the population response remained at the same location with much the same shape in Fig. 2a, but with an amplitude that varied with background amplitude in an approximately linear way (Fig. 2b). Thus, the background modulated the amplitude of the tuning curve of each neuron. For comparison, an example of gain modulation observed in posterior parietal cortex[15] is shown in Fig. 2c. The tuning curve indicates that the neuron is selective for the location of a visual stimulus in retinotopic coordinates, while the amplitude of response linearly encodes the position of the eyes. In a previous model of gain modulation, it was assumed that excitatorily coupled neurons in parietal cortex share the same efference copy of eye position, which amounts to a uniform background input[7].

Whereas the foreground stimulus and the background cooperate to determine the response of the circuit in Fig. 2, two localized stimuli compete to determine the response in Fig. 3. The circuit selects one of the stimuli while completely suppressing its response to the other (Fig. 3a, b). When the amplitudes of the two stimuli are sufficiently different from each other, the circuit always selects the larger stimulus. This property is evident in the hysteresis curve (Fig. 3c), which has a single branch at the extremes. By contrast, when the stimuli have roughly equal amplitudes, the circuit may select either one stimulus or the other. In this bistable regime, once a choice has been made, the circuit maintains its past selection and is insensitive to small changes in relative amplitudes of the stimuli. Bistability enables the neurons to maintain a memory of the past, but in spite of bistability, the neural firing rates remain continuously graded. For example, if the amplitudes of the stimuli are rescaled by the same factor, then the response amplitude is similarly rescaled. On the other hand, in Fig. 3d, when the stimuli marked by asterisks are moved closer to each other, then the circuit tends to interpolate between them rather than to select one of them. The network

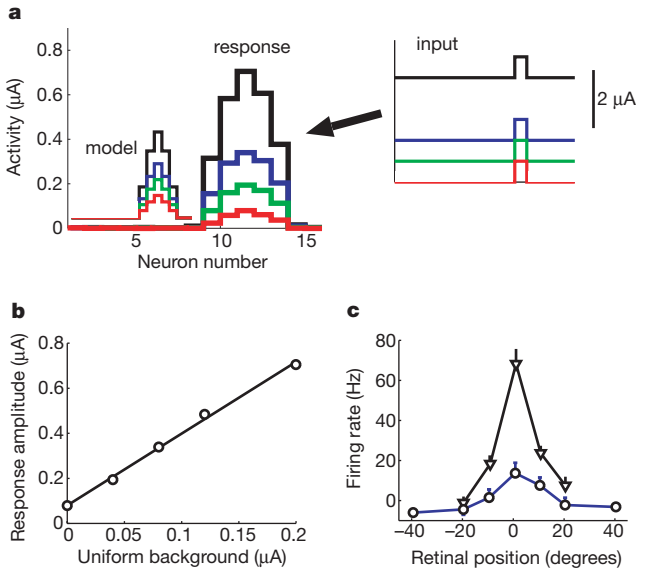

Figure 2 Modulation of tuned population response. $V_{\alpha_{-1}} = 5$ mV, $V_{\alpha_1} = 6$ mV, $V_{\alpha_{-2}} = 5$ mV, $V_{\alpha_2} = 9$ mV, $V_{\alpha_0} = 88$ mV, $V_{\beta_i} = 11$ mV and $V_{\beta_0} = 6$ mV. **a**, The thick red line represents the response of the circuit to a single stimulus applied to neuron number 12. When a uniform background input is added, the response profile is modulated but its shape remains approximately invariant. The colours indicate which output profile corresponds to which input profile shown on the right. **b**, The response of neuron 12 in **a** is plotted versus the amplitude of the uniform background, resulting in a linear relationship. **c**, Gain modulation as observed in posterior parietal cortex (reproduced with permission from R. Andersen; ref. 15). Firing rates for two different eye positions are plotted as a function of the retinal horizontal eccentricity of a visual stimulus. Each data point is the average response to eight repetitions of the stimulus. Background activity before the stimulus presentation has been subtracted from the total activity during measurement.

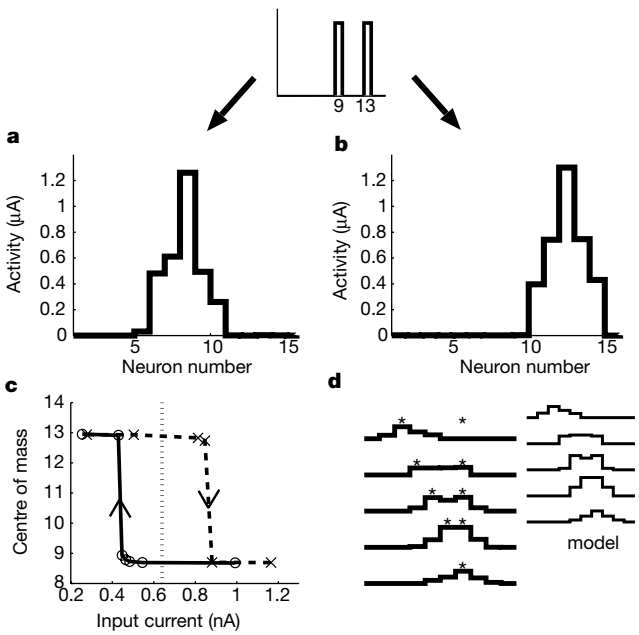

Figure 3 Multistability of selection. Synaptic strengths are the same as in Fig. 2. In response to two identical stimuli (inset, $V_{e_9} = V_{e_{13}} = 0.425$ V), the circuit selects one and suppresses the other. The left stimulus is selected in **a** and the right stimulus is selected in **b**. **c**, Hysteresis is evident in a graph of the response centroid. The intensity of the left stimulus (referred to as input current on the x-axis) is swept upward (dashed line) and then downward (solid line), whilst the intensity of the right stimulus is held fixed (dotted vertical line). **d**, Averaging versus selection. When two identical stimuli (asterisks) are nearby, then excitatory neurons in between the stimuli respond to their presence (lower traces). When the two stimuli are further apart, then the circuit selects one of the stimuli (here, the left stimulus, top trace).

interprets two nearby stimuli as a corrupted version of a single intermediate one, and restores its output towards the choice.

In trying to understand the analogue–digital nature of our specific circuit design, we have developed a general theory of recurrent networks with rectification nonlinearity and symmetric interactions. The starting point is a basic observation about the strength of feedback. Even if all synaptic strengths are kept fixed, the effective strength of feedback is variable. This property arises because the neurons of the network can be partitioned into two disjoint sets: those that are above threshold and active, and those that are below threshold and inactive. The effective strength of feedback depends only on the synaptic connections between active neurons, as only they participate in feedback loops. Depending on this effective strength, each active set can be classified as either 'forbidden' or 'permitted'. Forbidden sets are those for which feedback is strong enough to induce instability. A forbidden set cannot be realized by a stable steady state, no matter what external input is applied. In contrast, permitted sets are those for which feedback is weak enough that there are no instabilities. They can be realized by a stable steady state, given the proper pattern of external input. The fact that the stability of a steady state depends only on the identities of active neurons, and not on their analogue responses, is

Box 1

Theory of symmetric networks with rectification

In general, our current-mode design techniques can be used to implement electronic circuits that are approximately described by the dynamical equations

$$\tau_i(x_i)\frac{dx_i}{dt} + x_i = \left[b_i + \sum_j W_{ij}x_j\right]_+ \qquad (1)$$

Here the variables $\mathbf{x} = (x_i) \geq 0$ denote the output currents of neurons and $\mathbf{b} = (b_i)$ their input currents. The strength of the synaptic connection from the jth to the ith neuron is denoted by W_{ij} and $[x]_+ = \max(0,x)$ is a rectification nonlinearity. The time scales $\tau_i(x_i) \propto (x_i)^{-1}$ are inversely proportional to the x_i, which is a basic property of current-mode circuits. For the proofs of the results to follow, see Supplementary Information.

Effective gain at steady state

We assume that the inputs $\mathbf{b}$ are constant in time, and analyse the steady states $\bar{x}_i$ defined by $\frac{dx_i}{dt} = 0$. In such steady states, digital selection and analogue amplification can be separated from each other by using binary variables σ_i taking the values 1 or 0, depending on whether the ith neuron is active ($\bar{x}_i > 0$) or inactive ($\bar{x}_i = 0$).

$$\bar{\mathbf{x}} = G\mathbf{b}, \quad \text{where} \quad G = (I - \Sigma W\Sigma)^{-1}\Sigma \qquad (2)$$

is called the effective gain matrix[25]. I denotes the identity matrix and $\Sigma = diag(\sigma_1, \ldots, \sigma_N)$ is a matrix that carries 'digital' information about which neurons are active ($\sigma_i = 1$ if neuron i is active and zero otherwise). The effective gain G depends on the identities of the active neurons, though it is independent of their analogue responses. It is composed of two factors. One factor $(I - \Sigma W\Sigma)^{-1}$ quantifies the feedback amplification mediated by the synaptic connections between active neurons (the expression $\Sigma W\Sigma$ is like W, except that the strengths of all synapses involving inactive neurons are zeroed out). The other factor, Σ, signifies that only the inputs to active neurons are amplified.

Global stability if no unstable common mode

Do the dynamics in equation (1) always converge to a steady state? In the case of some symmetric networks ($W_{ij} = W_{ji}$), the answer is yes. Global stability can be proven if $\Sigma W\Sigma$ has no unstable common modes for any Σ, where a common mode is an eigenvector whose components all have the same sign and instability means that the corresponding eigenvalue is larger than one. Intuitively, unstable common modes lead to runaway excitation, incompatible with global stability.

On the other hand, a differential mode of $\Sigma W\Sigma$ is an eigenvector with both positive and negative components. In contrast to common modes, a differential mode can be unstable and not cause any harm to the global stability of a network. The growth of unstable differential modes necessarily makes some neurons hit rectification nonlinearity. As we will see, this turns out to be beneficial for stability.

Local stability is independent of analogue response values

The local stability of steady states can be determined by linearizing the dynamics about $\bar{\mathbf{x}}$,

$$\frac{d\mathbf{x}}{dt} = -D(\bar{\mathbf{x}})^{-1}(I - \Sigma W\Sigma)(\mathbf{x} - \bar{\mathbf{x}}) \qquad (3)$$

where $D(\bar{\mathbf{x}}) = diag\,\tau_1(\bar{x}_1), \ldots, \tau_N(\bar{x}_N))$. Using the assumption of a symmetric W, local stability follows if the largest eigenvalue of $\Sigma W\Sigma$ is bounded above by unity (it can be proven that the factor $D(\bar{\mathbf{x}})^{-1}$ does not matter). This means that the stability of a steady state depends on the set of active neurons, but does not depend on their analogue responses. In practice, only stable steady states can be observed in a network, because even infinitesimal amounts of noise cause divergence from an unstable steady state. However, differential instabilities are essential for digital constraints on selection, because they are necessary for the existence of forbidden sets.

The grouping into permitted and forbidden sets

If the largest eigenvalue of $\Sigma W\Sigma$ is greater than unity for some set of active neurons defined by Σ, we refer to that set as a 'forbidden set'. On the other hand, if the largest eigenvalue is bounded above by unity, the active set is 'permitted'. It can be shown that for every permitted set, there exists a stimulus vector $\mathbf{b}$ that produces a stable steady state response consistent with that set.

Our main result is that in a symmetric network, any subset of a permitted set is permitted and any superset of a forbidden set is forbidden. Proof: this grouping follows from the fact that the largest eigenvalue of $\Sigma W\Sigma$ is always smaller than that of W. The largest eigenvalue of W can be characterized by using the Rayleigh–Ritz quotient[26]:

$$\lambda_{max} = \max_{\mathbf{v}} \frac{\mathbf{v}^T W\mathbf{v}}{\mathbf{v}^T\mathbf{v}} \qquad (4)$$

Similarly, the largest eigenvalue of $\Sigma W\Sigma$ is given by maximizing the same expression, but constraining $v_i = 0$ for the inactive neurons. As imposing more constraints cannot increase the maximum, it follows that inactivating a neuron cannot increase the strength of positive feedback and therefore cannot enhance instability. Intuitively, both mutual excitation and mutual inhibition constitute positive feedback and so explain this hierarchical grouping of permitted sets.

For the mathematical model of our circuit with the parameters given in the Methods section, any active set consisting of more than five contiguous neurons is a forbidden set, and so sets a maximal response width (this result was derived by numerically diagonalizing $\Sigma W\Sigma$).

No multistable selection without differential instabilities

The circuit illustrated in Figs 2 and 3 is potentially multistable, in the sense that there exists at least one input vector $\mathbf{b}$ allowing for more than a single stable steady state. In general, the existence of differential instabilities is necessary and sufficient for potential multistability. This can be proven using Lyapunov function arguments. Intuitively, multistability occurs when there is more than one local minimum of the Lyapunov function. In this situation, saddles exist between the multiple minima, indicating that there are unstable differential modes.

a specific consequence of rectification nonlinearity (Box 1).

In the course of converging to a steady state, the dynamics of a network of N neurons must select one of the 2^N possible active sets. The existence of forbidden sets gives the selection process a digital character, meaning that the active sets at steady state obey hard constraints. Most importantly, the constraints cannot be violated, no matter what the external input may be. In general, varying the recurrent synaptic strengths of a network causes these constraints to change. In particular, if synaptic feedback is weak, then there may be no forbidden sets at all. Similarly, networks with different patterns of synaptic connectivity generally implement different constraints. However, this flexibility has its limits, as the constraints cannot take an arbitrary form. It can be shown that any subset of a permitted set is permitted, and any superset of a forbidden set is forbidden (Box 1).

Given that the network dynamics has selected a permitted set, the analogue outputs of the active neurons are related to their inputs by an effective gain matrix, which quantifies the amplification or attenuation produced by the feedback connections between the active neurons. As explained earlier, inactive neurons and their synaptic connections are irrelevant. The effective gain depends on the identities of the active neurons only, though it does not depend on their analogue responses. The result is that steady states with the same active set behave like the responses of a linear system, but nonlinearities emerge when different active sets are compared with each other.

This general theory is applicable to our circuit in Figs 2 and 3, where there is approximate symmetry of the synaptic interactions (in the case of nonsymmetric interactions, the theory does not apply because there can be spontaneous generation of spatiotemporal activity patterns; see Supplementary Information). Due to local cooperation and lateral competition, the number of contiguous neurons in a permitted set is limited and so activity profiles cannot exceed a maximal width. This does not mean that there is a similar constraint that prevents the narrowing of an activity profile. Narrowing can be achieved, for example, by applying a feedforward input i (Fig. 1) to the inhibitory neuron. This property follows from our earlier statement that every subset of a permitted set is also a permitted set and is the reason why the response does not broaden in Fig. 2, even when the input becomes almost completely uniform[5,7,16]. Intuitively, a uniform, nonspecific input transiently excites the most unstable mode in any symmetric network and so is a computational means of enforcing selection of a permitted set comprising many active neurons. The suppression of the response to one stimulus in Fig. 3a and b can also be understood as the outcome of constrained selection. Constraints also cause the circuit to interpret two nearby stimuli as a corrupted version of a single, intermediate stimulus (Fig. 3d).

The constraints that define the maximal response width to stimulation can be made more or less restricted by changing the synaptic strengths. For example, if the strengths of lateral excitation are adjusted to zero, leaving only self-excitation, then the only permitted sets are those with a single neuron active, so that the circuit functions in a winner-take-all mode[17–19].

The concept of effective gain is useful for understanding the analogue behaviours observed in Figs 2 and 3. In Fig. 2a, the set of active neurons remains basically the same for all stimuli, so that the effective gain is constant, explaining the linearity of Fig. 2b. By contrast, the active sets are completely different in Fig. 3a and b, and so are the effective gains, which explains why the response is so nonlinear.

The multistability shown in Fig. 3 is reminiscent of the flip-flop, a digital feedback circuit consisting of two elements interacting by mutual inhibition. The feedback creates differential instability, which drives the voltages of the two elements to opposite limits of the power supply. This is why the flip-flop is constrained to two possible states, and is bistable. Similarly, in our general theory of recurrent networks, the existence of differential instabilities is necessary for constrained selection, and the possibility of multistability (Box 1). But these networks differ from the flip-flop, in that growth of instabilities is limited by threshold nonlinearity alone. No saturation or upper limit on activity is necessary to hold instabilities in check. That is why digital selection can coexist with analogue response.

Our theory of recurrent networks is related to, but distinct from, the paradigm of computation with dynamical attractors[20,27]. According to the attractor model, memories are stored as stable fixed points, or dynamical attractors of a recurrent neural network. External input serves only to initialize the network dynamics, which retrieves a stored memory by converging to an attractor. The attractor model was exciting because it provided a mathematically precise formulation of the intuitive idea that patterns can be latent in the recurrent connections of a network. Our theory provides a different formalization of the same intuitive idea. The permitted sets can be regarded as binary patterns stored in the recurrent connections. The identities of active neurons are determined by retrieving one of these stored memories. However, this retrieval does not fix the analogue responses of the active neurons. These arise from feedback amplification and attenuation of the maintained external input.

In our circuit, the permitted sets are simply groups of neighbouring neurons. However, permitted sets can take more complex forms in circuits with more sophisticated synaptic connectivity. For example, we can imagine a computational role for permitted sets in a network for visual recognition of letters of the alphabet. This network would contain neurons that represent the strokes of which letters are composed. Then co-activation of the neurons in a permitted set would represent a letter as a combination of strokes. Other combinations that do not correspond to letters would be forbidden by the recurrent connections. More generally, in parts-based representations of objects[21], forbidden sets could impose 'syntactic' constraints on the way that parts are combined to form a whole. But analogue variability is also an important property of perceptual stimuli. Changes in viewpoint, lighting, and other factors can cause continuous variations in the image of an object. As both analogue computation and digital constraints coexist in our circuits, they are potentially well suited for applications to machine perception and efficient hybrid computations[22]. To build such circuits, it will be important to devise mechanisms of synaptic plasticity, so that parts-based representations for perception can be learned. □

Methods

Our circuit was fabricated using the 2 μm process of the MOSIS facility. Bipolar transistors were used, as well as MOSFETS (metal oxide semiconductor field effect transistors) because in weak inversion current mirrors made from bipolar transistors have superior matching and a larger linear range than those made from MOSFETS. We have used a current-mode design, which is a suitable technique for implementations of neural circuits[23]. In addition to the ring network of Fig. 1, the chip included digital circuitry for scanning the multiple currents of the excitatory neurons[24] out through a single current-sense amplifier.

We can derive model equations for the currents E_k of excitatory neurons and I of the inhibitory neurons (see Fig. 1). By substituting the current–voltage relationship $E_k = I_0 e^{\kappa V_G/U_T}$ of a CMOS (complementary metal-oxide semiconductor) transistor ($\kappa \approx 0.7$ is the gate efficiency constant, $U_T \approx 25$ mV is the thermal voltage and I_0 is the dark current) into $I_{in} - E_k = C\frac{dV_G}{dt}$ for the gate voltage V_G of the rectification mirror (here V_G is referenced to VDD) we obtain the output currents E_k ($k = 1, \ldots, N$) of the $N = 16$ excitatory neurons:

$$\frac{C}{E_k}\frac{dE_k}{dt} + E_k = \left[e_k + \sum_{l=-2}^{2} \alpha_l E_{k+l} - \beta I\right]_+ \quad (5)$$

$$I = i + \sum_{k=1}^{N} E_k \quad (6)$$

In this derivation, $E_{N+l} = E_l$ has been defined and $C > 0$ is a constant depending on the capacitance of the rectification mirror. Our measurements indicate that equations (5) and

(6) are valid for output currents ranging over six orders of magnitude, from 1 nA to tens of mA of current.

The excitatory neurons interact by self (α_0), nearest neighbour (α_1 and α_{-1}), and next nearest neighbour (α_2 and α_{-2}) connections. The inhibitory neuron I sums the currents from the excitatory neurons, and in turn inhibits them with a strength β. The strength α_l of each type of excitatory synapse is globally controlled by the emitter voltage V_{α_l}, and the strength β of inhibition is globally controlled by the difference $V_{\beta_i} - V_{\beta_0}$: $\alpha_l = e^{-V_{\alpha_l}/U_T}$ and $\beta = e^{(V_{\beta_i} - V_{\beta_0})/U_T}$ (the emitter voltages are references to a variable cell ground). Similarly, the input currents e_k and i to excitatory and inhibitory neurons are exponentially related to externally controlled voltages V_{e_k} and V_i. A synaptic weight can be turned off by setting the emitter voltage to about 1V, where it is above the base voltage, under which conditions current cannot flow across the bipolar.

In excitatory–inhibitory networks, it is known that slow inhibition can lead to oscillatory or explosive instability. Therefore we sped up inhibition by buffering the current mirrors of the inhibitory synapses ('buffered output' in Fig. 1c, bf_bias = 3.5 V), and we slowed down excitation by adding a large capacitance to the current mirror of the excitatory neurons. In equation (6), the speed of inhibition was approximated as instantaneous.

We were able to reproduce the measurements shown in Figs 2 and 3 by simulating the model equations (5) and (6) with parameter values $\alpha_0 = 0$, $\alpha_{-1} = \alpha_1 = 1.15$, $\alpha_{-2} = \alpha_2 = 8$ and $\beta = 0.5$. The parameters of the model were tuned to match the response profiles. Although we tried to minimize the mismatch between different neurons and synapses by a generous layout in terms of transistor and capacitor size, there are small inhomogeneities owing to imperfections of the fabrication process.

Received 27 December 1999; accepted 13 April 2000.

1. Leopold, D. A. & Logothetis, N. K. Activity changes in early visual cortex reflect monkeys percepts during binocular rivalry. *Nature* **379,** 549–553 (1996).
2. Treue, S. & Maunsell, J. H. Attentional modulation of visual motion processing in cortical areas MT and MST. *Nature* **382,** 539–541 (1006).
3. Treue, S., Martinez, S. & Trujillo, J. C. Feature-based attention influences motion processing gain in macaque visual cortex. *Nature* **399,** 575–579 (1999).
4. Reynolds, J. H., Chelazzi, L. & Desimone, R. Competitive mechanisms subserve attention in macaque areas V2 and V4. *J. Neurosci.* **19,** 1736–1753 (1999).
5. Ben-Yishai, R., Lev Bar-Or, R. & Sompolinsky, H. Theory of orientation tuning in visual cortex. *Proc. Nat. Acad. Sci. USA* **92,** 3844–3848 (1995).
6. Hansel, D. & Sompolinsky, H. in *Methods in Neuronal Modeling* (eds Koch, C. & Segev, I.) 499–567 (MIT Press, Cambridge, Massachusetts, 1998).
7. Salinas, E. & Abbott, L. F. A model of multiplicative neural responses in parietal cortex. *Proc. Natl Acad. Sci. USA* **93,** 11956–11961 (1996).
8. Georgopoulos, A. P., Taira, M. & Lukashin, A. Cognitive neurophysiology of the motor cortex. *Science* **260,** 47–52 (1993).
9. Camperi, M. & Wang, X. J. A model of visuospatial working memory in prefrontal cortex: recurrent network and cellular bistability. *J. Comput. Neurosci.* **5,** 383–405 (1998).
10. Zhang, K. Representation of spatial orientation by the intrinsic dynamics of the head-direction cell ensemble: A theory. *J. Neurosci.* **16,** 2112–2126 (1996).
11. Kopecz, K. & Schoner, G. Saccadic motor planning by integrating visual information and pre-information on neural dynamical fields. *Biol. Cybern.* **73,** 49–60 (1995).
12. Amari, S.-I. & Arbib, M. A. in *Systems Neuroscience* (ed. Metzler, J.) 119–165 (Academic Press, New York, 1977).
13. Seung, H. S. & Sompolinsky, H. Simple models for reading neuronal population codes. *Proc. Natl Acad. Sci. USA* **90,** 10749–10753 (1993).
14. Abbott, L. F. Decoding neuronal firing and modelling neural networks. *Q. Rev. Biophys.* **27,** 291–331 (1994).
15. Andersen, R. A., Essick, G. E. & Siegel, R. M. Encoding of spatial location by posterior parietal neurons. *Science* **230,** 456–458 (1985).
16. Amari, S.-I. Dynamics of pattern formation in lateral-inhibition type neural fields. *Biol. Cybert.* **27,** 77–87 (1977).
17. Lazzaro, J., Ryckebusch, S., Mahowald, M. A. & Mead, C. A. in *Advances in Neural Information Processing Systems* (ed. Touretzky, D. S.) 703–711 (Morgan Kaufmann, San Mateo, California, 1989).
18. De Weerth, P. & Morris, T. G. CMOS current mode winner-take-all circuit with distributed hysteresis. *Electron. Lett.* **31,** 1051–1053 (1995).
19. Indiveri, G. Winner-take-all networks with lateral excitation. *Analogue Integrated Circuits Signal Process* **13,** 185–193 (1997).
20. Amit, D. J. The Hebbian paradigm reintegrated: Local reverberations as internal representations. *Behav. Brain Sci.* **18,** 617–657 (1995).
21. Lee, D. & Seung, H. S. Learning the parts of objects by nonnegative matrix factorization. *Nature* **401,** 788–791 (1999).
22. Sarpeshkar, R., Lyon, R. F. & Mead, C. A low-power wide-dynamic-range analogue vlsi cochlea. *Analogue Integrated Circuits Signal Process.* **16,** 245–274 (1998).
23. Andreou, A. G. & Boahen, K. A. Synthetic neural circuits using current-domain signal representations. *Neural Computat.* **1** (1989).
24. Mead, C. & Delbrück, T. Scanners for visualizing activity of analogue VLSI circuitry. *Analogue Integrated Circuits Signal Process.* **1,** 93–106 (1991).
25. Hahnloser, R. H. R. About the piecewise analysis of networks of linear threshold neurons. *Neural Net.* **11,** 691–697 (1998).
26. Horn, R. A. & Johnson, C. R. *Matrix Analysis* (Cambridge Univ. Press, New York, 1985).
27. Hopfield, J. J. & Tank, D. W. Neural computations of decisions in optimization problems. *Biol. Cybern.* **52,** 141–152 (1985).

Supplementary information is available on *Nature*'s World-Wide Web site (http://www.nature.com) or as paper copy from the London editorial office of *Nature*.

Acknowledgements

We acknowledge the support of the Swiss National Science Foundation SPP Program, Lucent Technologies and MIT. We thank A. Andreou, J. Kramer, D. Lee, C. Brody, M. Fee, D. Tank, P. Sinha, S. Roweis and S.-C. Liu for discussions about the circuits and current-mode design.

Correspondence and requests for materials should be addressed to R.H. (e-mail: rh@ai.mit.edu).

Induction of neurogenesis in the neocortex of adult mice

Sanjay S. Magavi, Blair R. Leavitt* & Jeffrey D. Macklis

Division of Neuroscience, Children's Hospital, and Department of Neurology and Program in Neuroscience, Harvard Medical School, Enders 350, 320 Longwood Avenue, Boston, Massachusetts 02115 USA

Neurogenesis normally only occurs in limited areas of the adult mammalian brain—the hippocampus[1], olfactory bulb[2–4] and epithelium[5], and at low levels in some regions of macaque cortex[6]. Here we show that endogenous neural precursors can be induced *in situ* to differentiate into mature neurons, in regions of adult mammalian neocortex that do not normally undergo any neurogenesis. This differentiation occurs in a layer- and region-specific manner, and the neurons can re-form appropriate cortico-thalamic connections. We induced synchronous apoptotic degeneration[7,8] of corticothalamic neurons in layer VI of anterior cortex of adult mice and examined the fates of dividing cells within cortex, using markers for DNA replication (5-bromo-deoxyuridine; BrdU) and progressive neuronal differentiation. Newly made, BrdU-positive cells expressed NeuN, a mature neuronal marker, in regions of cortex undergoing targeted neuronal death and survived for at least 28 weeks. Subsets of BrdU+ precursors expressed Doublecortin, a protein found exclusively in migrating neurons[9,10], and Hu, an early neuronal marker[11,12]. Retrograde labelling from thalamus demonstrated that BrdU+ neurons can form long-distance corticothalamic connections. Our results indicate that neuronal replacement therapies for neurodegenerative disease and CNS injury may be possible through manipulation of endogenous neural precursors *in situ*.

There is precedent for neuronal death modifying the fate of immature precursor cells, but only in regions of the vertebrate brain that have ongoing neurogenesis. Direct[13–15] and correlative evidence[5,16,17] suggests that neuronal death can trigger increased neuron addition in these systems. Our previous results show that in regions of adult mouse neocortex undergoing synchronous apoptotic degeneration of projection neurons[7,8], the surrounding cells, including interneurons, upregulate the expression of a specific set of developmental signalling molecules that may guide neocortical projection neuron differentiation[18]. Immature neurons or multipotent neural precursors that are transplanted into these regions migrate selectively to layers of cortex where projection neurons are degenerating[7,8,19,20]. They then differentiate into projection neurons[7,8,15,19,20], receive afferent synapses[7,15,20] and re-form appropriate long-distance connections to the original contralateral targets of the degenerating neurons[19,20]. Similarly, induction of targeted neuronal death in projection neurons of the song circuitry in the avian forebrain causes increased neuron replacement from

* Present address: Center for Molecular Medicine and Therapeutics, Department of Medical Genetics, University of British Columbia, Vancouver, British Columbia V5Z 4H4, Canada.